Available online at www.sciencedirect.com
ScienceDirect
Trans. Nonferrous Met. Soc. China 30(2020) 2709−2723
Transactions of Nonferrous Metals Society of China
www.tnmsc.cn

Hot working characteristics of HEXed PM nickel-based superalloy during hot compression

Gang TAN[1], Hui-zhong LI[1], Yan WANG[2,3], Lei YANG[1], Shi-chang QIAO[3], Zheng-qin HUANG[3], Min-xue LIU[4]

1. School of Materials Science and Engineering, Central South University, Changsha 410083, China;
2. National Key Laboratory for Precision Hot Processing of Metals, Harbin Institute of Technology, Harbin 150001, China;
3. School of Aeronautics and Astronautics, Central South University, Changsha 410083, China;
4. State Key Laboratory of Powder Metallurgy, Central South University, Changsha 410083, China

Received 7 January 2020; accepted 17 August 2020

Abstract: To study the hot deformation behavior of a new powder metallurgy nickel-based superalloy, hot compression tests were conducted in the temperature range of 1020−1110 °C with the strain rates of 0.001−1 s^{-1}. It is found that the flow stress of the superalloy decreases with increasing temperature and decreasing strain rate. An accurate constitutive equation is established using a hyperbolic-sine type expression. Moreover, processing map of the alloy is constructed to optimize its hot forging parameters. Three domains of dynamic recrystallization stability and instability regions are identified from the processing map at a strain of 0.7, respectively. The adiabatic shear band, intergranular crack and a combination of intergranular crack and wedge crack are demonstrated to be responsible for the instabilities. Comprehensively analyzing the processing map and microstructure, the optimal isothermal forging conditions for the superalloy is determined to be t=1075−1105 °C and $\dot{\varepsilon}=10^{-3}$−$10^{-2.8}$ s^{-1}.

Key words: powder metallurgy; nickel-based superalloy; hot deformation behavior; constitutive equation; hot processing map; dynamic recrystallization

1 Introduction

Powder metallurgy (PM) nickel-based superalloy has become an irreplaceable key material for advanced aero-engine structural and heat-transmission components due to its fine grain, uniform microstructure, excellent strength and creep properties at high temperatures [1−4]. During hot processing of PM nickel-based superalloy, various defects, such as cracks, adiabatic shear band and flow localization are easy to emerge, which affect its hot working properties as well as service performance. It is known that hot processing parameters have important influences on the flow stress behavior of alloys. Previous studies [5−7] have also shown that strain rate, deformation temperature, strain and other parameters have significant impacts on adjusting the microstructure and properties of nickel-based superalloys. Therefore, investigation on hot compression behavior of PM nickel-based superalloys under different processing conditions is of great significance for designing and optimizing the hot working of the alloys.

It has been proven that the processing map developed on the basis of dynamic materials model (DMM) can help to predict the deformation mechanisms of superalloys under different conditions, optimize the related parameters of hot processing, and control microstructures [2,3,8−14].

Foundation item: Project (2016YFB0700300) supported by the National Key Research and Development Program of China; Project (51774335) supported by the National Natural Science Foundation of China
Corresponding author: Yan WANG, E-mail: wangyan@csu.edu.cn; Hui-zhong LI, E-mail: lhz606@csu.edu.cn
DOI: 10.1016/S1003-6326(20)65414-0

Extensive researches [3,8−10] have already been carried out on PM nickel-based superalloys by isothermal compression tests, in order to study their hot deformation behavior and processing maps. XU et al [3] studied the flow behavior and microstructural mechanism of a HIPed FGH96 superalloy, established the processing map according to the experimental data, and identified its optimum processing condition. NING et al [8] compared and analyzed the hot deformation behavior of FGH4096 superalloys with HIPed and fine-grained microstructures. It was found that different flow behaviors occurred in the superalloys due to different initial microstructures. Advanced processing maps were further established, and the differences in hot workability were also studied. SUI et al [9] investigated the processing map for hot working of Inconel 718 superalloy in the temperature range of 950−1150 °C and strain rate range of 0.001−100 s^{-1}. The results showed that the distribution of dynamic recrystallization zone in stable region is from lower temperature and lower strain rate to higher ones, and a peak efficiency of 0.39 occurs at about 950 °C and 0.001 s^{-1}. HE et al [10] investigated the constitutive relationship and processing map of a HIPed nickel-based powder superalloy during hot deformation, and suggested that due to formation of the adiabatic shear band, the instability in flow stress happened under the strain rate higher than 0.1 s^{-1} within the temperatures of 1000−1100 °C.

It is known that the initial state of an alloy would have an important influence on its hot working behavior. Although considerable literatures on hot deformation behavior of PM nickel-based superalloys have been published, the object of study mainly focused on the HIPed alloys. There are few reports concerning with hot working of HEXed PM nickel-based superalloys [11]. As one of the important alternative processing technologies for PM nickel-based superalloys, hot extrusion is expected to improve the forging microstructure of the alloy so that high-quality forging blanks can be obtained. The objective of this work is a new HEXed PM nickel-based superalloy. Compared to the second-generation PM nickel-based superalloys, the contents of cobalt (Co) and aluminum (Al) of the experimental alloy reach up to 26 wt.% and 3.2 wt.%, respectively. Previous results [15] have indicated that increasing the contents of Co and Al may improve phase stability, increase the volume of γ' solid solution and its solution temperature, and lower the quenching residual stress. This work aimed to systematically investigate the isothermal compression behavior of the HEXed PM nickel-based superalloy at the temperatures from 1020 to 1100 °C within the strain rates of 0.001−1 s^{-1}. The flow stress curves were corrected via an integrated method considering the friction and temperature variations during hot deformation. A constitutive equation and a flow stress model of strain compensation for hot compression of the superalloy were determined according to the corrected data, respectively. Hot processing maps under various strains were constructed, and instability and stability regions as well as their mechanisms were also analyzed combining with the corresponding microstructures, which can lay the foundation for the optimization of hot processing parameters of the superalloy.

2 Experimental

A recently developed PM nickel-based superalloy was used in this work with its compositions given in Table 1. Argon atomized powder was consolidated firstly by hot isostatic pressing at the temperature of 1100 °C under the pressure of 150 MPa for 4 h, and then by hot extrusion with a nominal extrusion ratio of 9:1. Before hot compression, the extruded bar was annealed at 900 °C for 2 h. Cylindrical samples of 8 mm in diameter and 12 mm in height were machined from the position of half of the radius for annealed bar to ensure the microstructural uniformity of all specimens. A Gleeble−3500 thermal simulator was used to conduct the isothermal compression tests in a high vacuum environment under the conditions of strain rates from 0.001 to 1 s^{-1} and temperatures between 1020 and 1110 °C. After being heated to the set deformation temperature at a rate of 10 °C/s, all the samples were held for 4 min to ensure the even temperature before isothermal compression tests. The samples were then compressed to a true strain of 0.7, and quenched in water to room temperature so as to retain the deformed microstructure. On both ends of the specimen, 0.05 mm thick graphite foils were added for reducing its friction with the indenter. Figure 1 illustrates the schematic diagram of the experimental setup and procedure for the tests.

Table 1 Chemical composition of experimental PM superalloy (wt.%)

Co	Cr	Ti	W	Mo	Al
26	13	3.7	4	4	3.2
Nb	Hf	C	B	Zr	Ni
0.95	0.2	0.05	0.025	0.05	Bal.

Both the extruded and the compressed samples were segmented along the direction of the compressive axis by a wire cut machine. After being ground and polished with a standard procedure, the samples were examined on a LEICA-DM4000M optical microscope and a FEI Quanta 650 field-emission gun scanning electron microscope (SEM), so as to analyze the evolution of grains and γ' precipitates, respectively. The etching agents for grain boundary and γ' precipitates are 100 mL HCl + 100 mL C_2H_5OH + 5 g $CuCl_2$ and 33 mL HNO_3 + 33 mL CH_3COOH + 33 mL H_2O + 1 mL HF, respectively. The mean-linear intercept method was used to measure the grain size of each sample by five metallographs taken from their central area. The size and volume fraction of γ' phase of the specimens were measured by Photoshop software and Image Pro Plus (IPP) software using ten SEM micrographs. The average values were determined to be the final data.

3 Result and discussion

3.1 Original microstructure

Figure 2 presents the initial microstructure of the experimentally annealed PM superalloy along the extrusion direction. Equiaxed grains with a distribution of bimodal size, namely, some large grains surrounded by small grains, are exhibited in the annealed alloy (Fig. 2(a)). The grain sizes are measured to be between 2 and 24 μm, and the average value is about 12 μm. A few residual prior particle boundaries (PPBs), which are characterized by black precipitates at the grain boundaries, can be observed as indicated by the arrows marked in Fig. 2(a). PPB has been reported to be the network structures which are mainly composed of micropores and carbide or carbon oxide precipitated around the original powder boundaries [12] of the PM superalloy during hot isostatic pressing. Although most of the PPB networks are broken and eliminated after hot extrusion, there is still a small portion of residual PPB located at the grain boundaries. γ' phase in the annealed alloy shows a

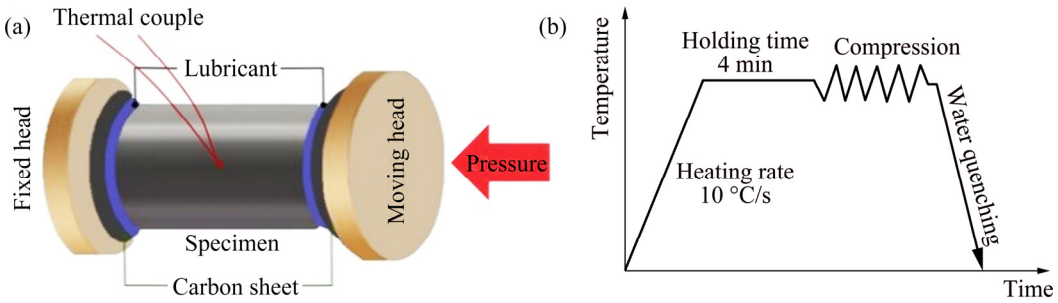

Fig. 1 Schematic diagrams showing experimental setup (a) and procedure (b) of hot compression tests

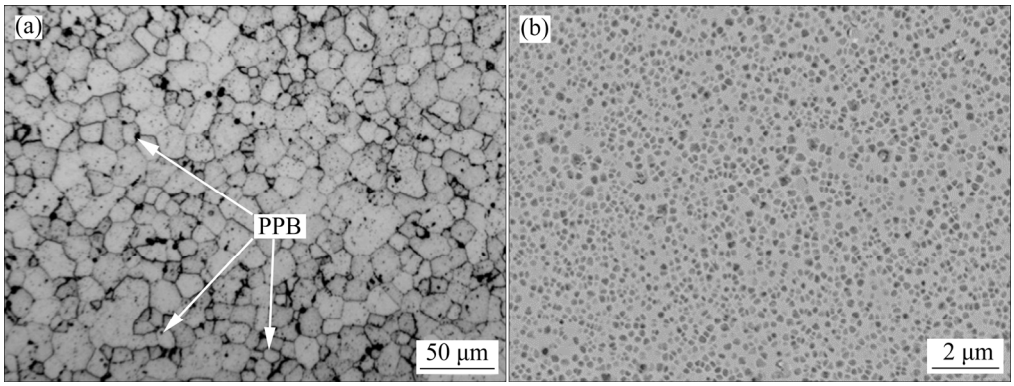

Fig. 2 Original microstructure of experimentally annealed PM superalloy: (a) Optical micrograph; (b) SEM image

spherical morphology, as seen from Fig. 2(b). Its size presents a unimodal distribution ranging from 145 to 215 nm, and its volume fraction is measured to be about 43.3%.

3.2 Flow behavior and friction correction

3.2.1 Original flow curves

The solid lines in Fig. 3 show the original true stress (σ)−true strain (ε) curves of the experimental superalloys under various deformation conditions. Typical characteristics of DRX are exhibited in all the curves, which conform with the flow behavior of other nickel-based superalloy under hot deformation conditions [2,9−11]. The flow stress presents a sharp increase with the increase of strain in a small strain range until the peak value is reached. Then, it gradually decreases to a stable state. Such a behavior of flow stress during hot deformation implies a competitive process of dynamic softening and work hardening. Accompanied by increasing dislocation density in the initial stage of deformation, the hot working process is dominated by work hardening, resulting in a fast rise in stress. With gradual increase of strain, DRX occurs in the superalloy, which enhances the dynamic softening effect. Therefore, after reaching the peak value, the flow stress gradually decreases since the dynamic softening becomes dominant in the deformation process [11]. A steady state of flow curve for the superalloy can be obtained ultimately under the conditions with lower strain rates, indicating that an equilibrium has been attained between work hardening and dynamic softening.

It may be noted from Fig. 3 that at higher strain rates (i.e. 0.1 or 1 s^{-1}), the experimental superalloys exhibit an abnormal flow behavior. Discontinuous flow softening characteristics, i.e. two peak stresses, are observed in the flow stress curves. It is suggested that as the deformation proceeds, the increase in dislocation density leads to initially rising in flow stress. When the dislocation density in the alloy accumulates to the critical value required for DRX to occur, the flow stress decreases slightly. However, due to the presence of a small portion of PPB at the grain

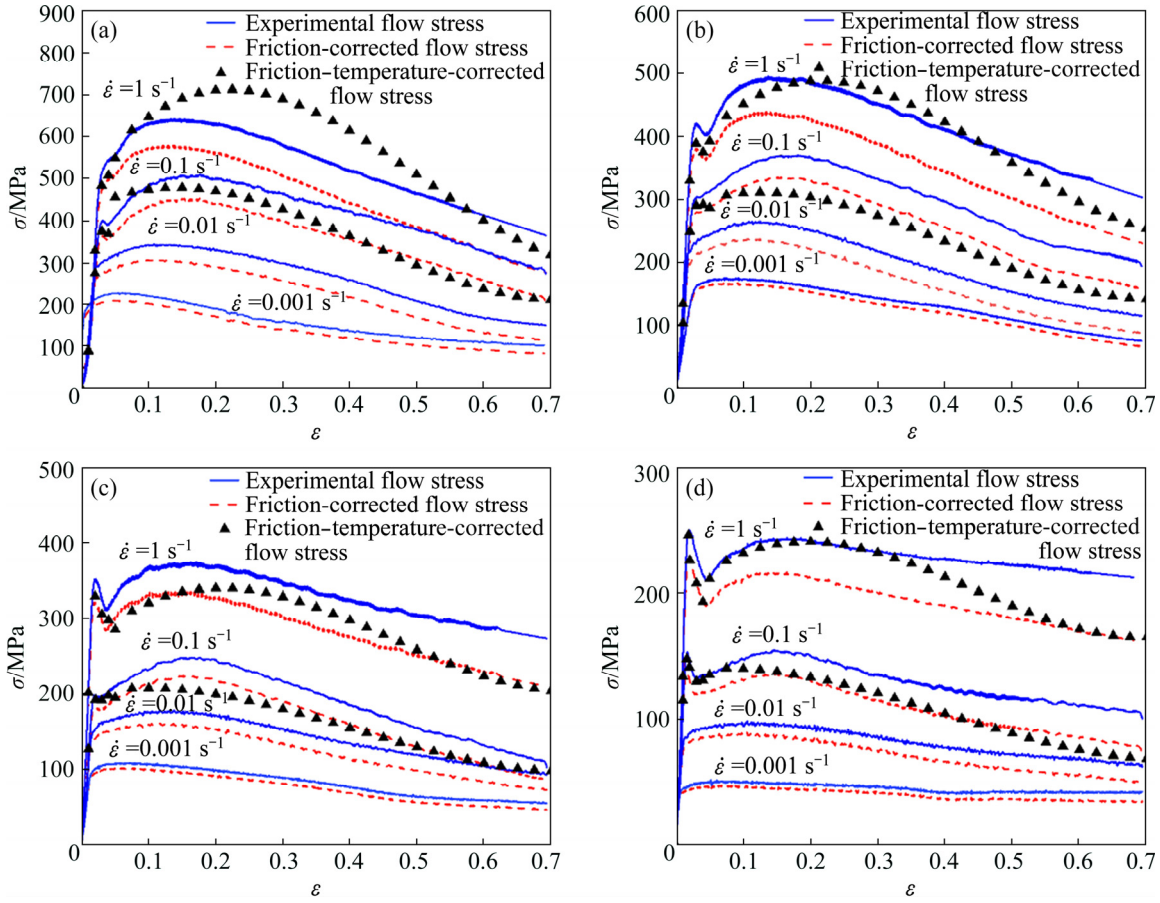

Fig. 3 Original and corrected flow curves of experimental superalloy compressed at different temperatures: (a) 1020 °C; (b) 1050 °C; (c) 1080 °C; (d) 1110 °C

boundary (see Fig. 2(a)), further nucleation of DRX will be hard since the dislocation density is too low to stimulate it. As a result, a decrease of flow stress appears after reaching the first peak stress. During the subsequent compression, with the dislocation density accumulating, the second peak stress appears, and PPB can become the nucleation sites of DRX owing to the development of the bulge and corrugation of PPB [16]. Therefore, DRX will continue until stable flow stress is obtained.

As seen from Fig. 3, the flow behavior of the experimental superalloys is significantly affected by both deformation temperature and strain rate. With rising temperature or declining strain rate, the flow stress decreases, which is typical for most nickel-based superalloys [10,12]. It is because under the same strain rate, DRX can be facilitated by increasing the temperature, and sufficient time can be provided for dislocation annihilation under lower strain rates at a certain temperature [17].

3.2.2 Friction correction

During the Gleeble tests, two factors that significantly affect true stress−true strain curves should be taken into consideration, i.e. the friction on the contact surface between cylindrical sample and indenter, and the temperature rise caused by plastic deformation.

Although the end face of the specimen was lubricated by the graphite foils and lubricant during the tests, the drum belly phenomenon of the specimen still appears because of the friction on the surfaces. The existence of frictional force makes the radial flow of the contact surface limited, leading to a change of the unidirectional stress state of the specimen. An error of the true stress−true strain curve is thus generated. Usually, a drum coefficient B (B is dimensionless) is used to judge whether the friction correction of true stress−true strain curve is necessary, which can be expressed as [18]

$$B=\frac{hR_{\mathrm{M}}^2}{h_0R_0} \tag{1}$$

where h_0 is the initial height, R_0 is the initial radius of cylinder, h is the height of the deformed specimen, and R_{M} is the maximum radius of the deformed specimen. The B value under each deformation condition in this experiment is calculated according to Eq. (1) by measuring the sample size before and after hot compression tests, which is exhibited in Table 2.

Table 2 B values for experimental superalloys deformed under different conditions

$\dot{\varepsilon}$ /s^{-1}	B			
	1020 °C	1050 °C	1080 °C	1110 °C
0.001	1.242	1.135	1.165	1.221
0.01	1.287	1.275	1.267	1.231
0.1	1.248	1.245	1.258	1.316
1	1.261	1.254	1.268	1.261

All the B values are greater than 1.1, as seen in Table 2. Since the error due to friction is thought to be large enough when $B\geq1.1$ [18], the flow curves of the experimental alloy need to be corrected so as to guarantee the accuracy of results. The friction correction method for flow stress curves used in this work was proposed by EBRAHIMI and NAJAFIZADEH [19]. Its expression is as follows:

$$\frac{\sigma_0}{\sigma}=8b\frac{R_{\mathrm{I}}}{H}\left\{\left[\frac{1}{12}+\left(\frac{H}{R_{\mathrm{I}}}\right)^2\frac{1}{b^2}\right]^{3/2}-\left(\frac{H}{R_{\mathrm{I}}}\right)^3\frac{1}{b^3}-\frac{\mu}{24\sqrt{3}}\frac{\exp(-b/2)}{\exp[(-b/2)-1]}\right\} \tag{2}$$

$$R_{\mathrm{I}}=R_0\sqrt{\frac{h_0}{h}} \tag{3}$$

$$b=4\frac{(R_{\mathrm{M}}-R_{\mathrm{T}})}{R_{\mathrm{I}}}\frac{H}{(h_0-H)} \tag{4}$$

$$R_{\mathrm{T}}=\sqrt{\frac{3h_0R_0^2}{H}-2R_{\mathrm{M}}^2} \tag{5}$$

where σ_0 and σ are the stresses before and after the friction correction, respectively; b is the barreling parameter; R_{I} is the instantaneous radius of the deformed specimen; H is the instantaneous height of deformed specimen; μ is the shear friction coefficient; R_{T} is the contact surface radius of the deformed specimen. The flow stress curves of the experimental superalloy after friction correction are shown in Fig. 3 in the dotted lines. It may be noted that the flow curves after friction correction are below the experimental ones, and the difference increases with the increasing strain. The regularity obtained above is consistent with the friction correction law reported in Ref. [9]. Since the radial flow of the specimen is hindered due to the friction effects, the compression process should be triggered with a higher pressure.

3.3 Constitutive equation and temperature rise correction

3.3.1 Temperature rise during hot compression

During hot deformation of superalloys, part of the work generated by plastic deformation is stored, causing the microstructure transformation. But most of the work will transform into heat energy owning to a low thermal conductivity of superalloy, resulting in the temperature rising. Especially, at higher strain rates, the internal temperature of specimen changes rapidly due to the short deformation time, so the actual temperature of the material is higher than the initial set one. The dynamic softening therefore occurs faster and the flow stress is lowered [20]. Generally, the rise of adiabatic temperature can be obtained based on the theoretical methods when the temperature of the material continues to rise during the process of continuous thermal deformation [21]. However, since the heat radiation and the heat transfer between the material and the indenter will cause the temperature of the specimen to drop during the actual deformation, it is difficult to quantify the temperature change during the deformation process by theoretical calculation.

Gleeble thermal simulator tester can instantly monitor the temperature change of the specimen through the welded thermocouple, adjust the current in the specimen, and reduce its temperature rise [22]. Figure 4 shows the temperature changes of the experimental superalloys during hot deformation detected by the thermocouples. It is found that with strain rate decreasing, the Gleeble system can effectively adjust the temperature of the specimen by reducing the current to compensate for the temperature rise. The temperature of specimen can be maintained at the set temperature at a strain rate of 0.01 s^{-1} after the strain reaches 0.1, and the specimen almost remains the set temperature under 0.001 s^{-1}. Thus, the internal temperature of samples deformed at 0.01 and 0.001 s^{-1} is considered to be evenly distributed. For the specimens deformed at the strain rates of 0.1 and 1 s^{-1} (Fig. 4), the temperature fluctuates apparently as the strain increases, especially for that at 1 s^{-1}. Meanwhile, the fluctuation becomes more pronounced at lower temperatures. Thus, further correction of temperature rise is still needed for the friction-corrected flow stresses of the specimens deformed at 0.1 and 1 s^{-1}.

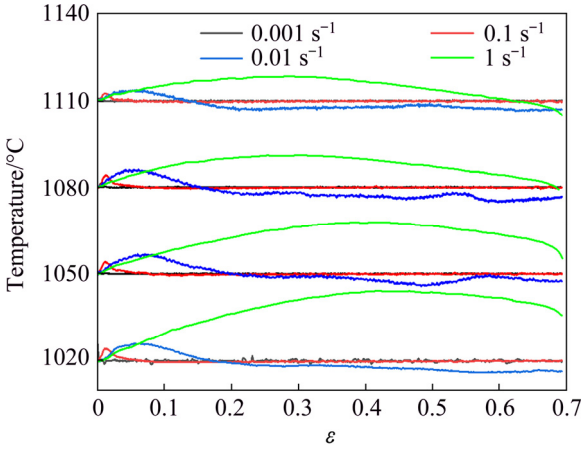

Fig. 4 Variation of detected temperature with strain under different deformation conditions

3.3.2 Constitutive equation corrected by temperature rise

During hot deformation, constitutive model of the flow stress is important for hot processing of an alloy from the metallurgical standpoint, because a relatively accurate flow description is the basis of effective mathematical simulation. Extensive researches on different materials have indicated that hot deformation is a process controlled by thermal activation. The equation proposed by SELLARS and MCTEGART [23], ZENER and HOLLOMON [24] is widely used to clarify the dependence of peak stress on strain rate and temperature, as shown in the following equations:

$$Z=\dot{\varepsilon}\exp\left(\frac{Q}{RT}\right)=A_1\sigma^n \tag{6}$$

$$Z=\dot{\varepsilon}\exp\left(\frac{Q}{RT}\right)=A_2\exp(\beta\sigma) \tag{7}$$

$$Z=\dot{\varepsilon}\exp\left(\frac{Q}{RT}\right)=A[\sinh(\alpha\sigma)]^n \tag{8}$$

where Z is the Zener–Hollomon parameter; $\dot{\varepsilon}$ is the strain rate, n is the stress multiplier; A_1, A_2, A, β and α represent the material constants; Q denotes the activation energy for hot deformation; R is the mole gas constant (8.314 J/(mol·K)); T represents the thermodynamic temperature.

For the purpose of correcting the temperature variation of the alloy deformed at higher strain rates, linear interpolation of $\ln\sigma$ and $1/T$ was calculated by Eq. (6) using the peak stress σ_p gained from the friction-corrected flow stress curves (see Fig. 4).

Combining the variation of the detected temperature (Fig. 4), the values of stresses were corrected by temperature rise [9], which corresponded to the strains at intervals of 0.02 under the strain rates of 0.1 and 1 s^{-1}, as shown in Fig. 3. It is found that although the shape of the corrected flow curves is similar to that before correction, non-negligible differences are still exhibited.

Assuming the activation energy (Q) to be a constant at a certain temperature, taking the logarithm of Eqs. (6) and (7), substituting the stress data corrected by temperature rise into the formulas, the constants of n and β are gained by linear fitting of $\sigma_p - \ln\dot{\varepsilon}$ and $\ln\sigma_p - \ln\dot{\varepsilon}$ plots (Figs. 5(a) and (b)), respectively. The value of constant α ($\alpha=\beta/n$) is then obtained. Under the conditions of certain temperatures or strain rates, Q can be given by differentiating Eq. (8) as follows:

$$Q = R\left(\frac{\partial \ln\dot{\varepsilon}}{\partial \ln[\sinh(\alpha\sigma)]}\right)_T \left(\frac{\partial \ln[\sinh(\alpha\sigma)]}{\partial(1/T)}\right)_{\dot{\varepsilon}} \quad (9)$$

where

$$\left(\frac{\partial \ln\dot{\varepsilon}}{\partial \ln[\sinh(\alpha\sigma)]}\right)_T \text{ and } \left(\frac{\partial \ln[\sinh(\alpha\sigma)]}{\partial(1/T)}\right)_{\dot{\varepsilon}}$$

are the average slopes of the $\ln\dot{\varepsilon} - \ln[\sinh(\alpha\sigma_p)]$ plots at various temperatures and the $\ln[\sinh(\alpha\sigma_p)] - 1/T$ plots at different strain rates (Figs. 5(c) and (d)), respectively. Therefore, combining Eq. (8) and linear fitting, α, Q, n and A can be determined as 0.0016108, 1111.3 kJ/mol, 5.1035 and 8.0348×10^{43}, respectively.

It can be seen from Fig. 6 that $\ln[\sinh(\alpha\sigma_p)]$ and $\ln Z$ exhibit a good linear relationship, and the linear correlation coefficient reaches 0.982. Therefore, the hyperbolic-sine function obtained below can better express the relationship between flow stress and deformation conditions during thermal deformation of the experimental superalloy.

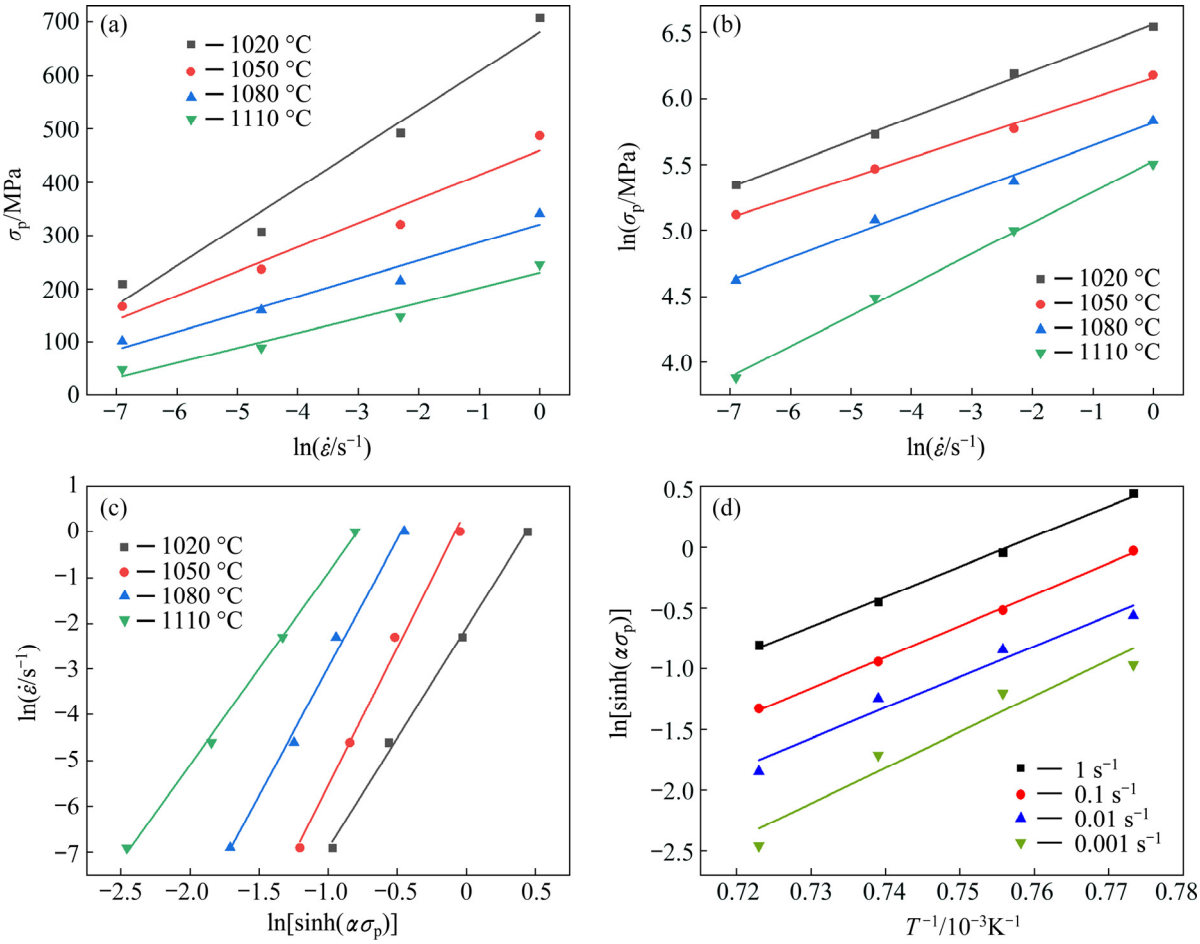

Fig. 5 Relationship between peak stress (σ_p) and strain rate ($\dot{\varepsilon}$) or temperature (T) for experimental superalloy during hot compression: (a) $\sigma_p - \ln\dot{\varepsilon}$; (b) $\ln\sigma_p - \ln\dot{\varepsilon}$; (c) $\ln\dot{\varepsilon} - \ln[\sinh(\alpha\sigma_p)]$; (d) $\ln[\sinh(\alpha\sigma_p)] - 1/T$

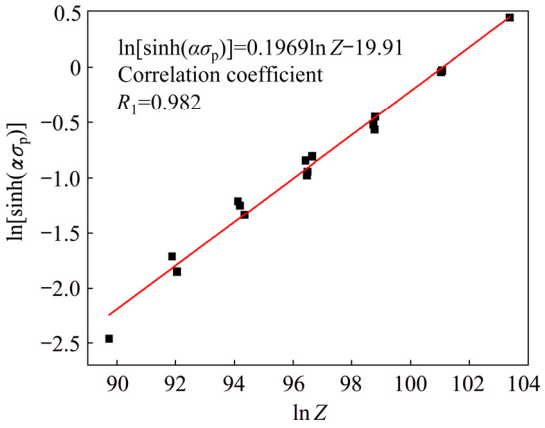

Fig. 6 Relationship between peak stress (σ_p) and Z parameter for experimental superalloy

$$\dot{\varepsilon}\exp\left(\frac{1111300}{RT}\right)= 8.0348\times10^{43}[\sinh(0.0016108\sigma)]^{5.1035} \quad (10)$$

The average activation energy Q of the experimental superalloy is higher than that of the reported superalloy with similar compositions [25]. It is known that the value of Q is influenced by various factors, including material composition, processing history and microstructure. On one hand, the higher value of Q for the superalloy is closely related to the increasing content of Co [26]. As the main alloy element of solid solution, Co atoms can substitute Ni atoms during material preparation, leading to a reduction of atomic order degree, so the diffusion activation energy of the alloy would be increased [27]. Since the self-diffusion may be involved in the thermal compression process of Ni−Co-based alloys [28], the value of Q would thus increase with the increasing Co content. On the other hand, the microstructural changes after hot extrusion, including reduction of the initial grain size [29], coarsening of the secondary γ' phase [30], as well as effective elimination of the inherent defects [9], have also important influences on the elevating of the deformation activation energy of the alloy.

3.3.3 Flow stress model of strain compensation

The flow stress in hot working process can be represented by the Z parameter through the transformation of Eq. (8):

$$\sigma=\frac{1}{\alpha}\ln\left\{\left(\frac{Z}{A}\right)^{\frac{1}{n}}+\left[\left(\frac{Z}{A}\right)^{\frac{1}{n}}+1\right]^{1/2}\right\} \quad (11)$$

According to Eq. (11) and the above method, the material parameters (n, A, α and Q) for the strains between 0.05 and 0.65 with an interval of 0.05 could also be determined, as shown in Fig. 7. By fitting the relationship between strain and parameters with the fifth-order polynomial, the flow stress model of the experimental superalloy that considers the effect of strain is established as follows:

$$\begin{cases}\sigma=\dfrac{1}{\alpha}\ln\left\{\left(\dfrac{Z}{A}\right)^{\frac{1}{n}}+\left[\left(\dfrac{Z}{A}\right)^{\frac{1}{n}}+1\right]^{1/2}\right\}\\ Z=\dot{\varepsilon}\exp\left(\dfrac{Q}{RT}\right)\\ n=6.3028-22.3258\varepsilon+124.2392\varepsilon^2-\\ \quad 326.7687\varepsilon^3+392.8011\varepsilon^4-170.0362\varepsilon^5\\ \ln A=126.96326-326.56948\varepsilon+1092.3694\varepsilon^2-\\ \quad 1437.1713\varepsilon^3-393.6709\varepsilon^4+1320.4490\varepsilon^5\\ \alpha=0.00369-0.0147\varepsilon-0.00854\varepsilon^2+\\ \quad 0.18795\varepsilon^3-0.46944\varepsilon^4+0.36876\varepsilon^5\\ Q/1000=1419.374-3771.93\varepsilon+10319.009\varepsilon^2-\\ \quad 4782.23\varepsilon^3-24999.06\varepsilon^4+27566.21\varepsilon^5\end{cases} \quad (12)$$

The predicted flow stress curves obtained by Eq. (12) together with the corrected flow curves are shown in Fig. 8. A good agreement is exhibited under different deformation conditions. Two statistical parameters, i.e. correlation coefficient R_1 and average absolute relative error (AARE), were introduced to further evaluate the accuracy of the predicted values, which can be defined as follows [31]:

$$R_1=\frac{\sum_{i=1}^{N}(X_i-\bar{X})(Y_i-\bar{Y})}{\sqrt{\sum_{i=1}^{N}(X_i-\bar{X})^2\sum_{i=1}^{N}(Y_i-\bar{Y})^2}} \quad (13)$$

$$\text{AARE}=\frac{1}{N}\sum_{i=1}^{N}\left|\frac{Y_i-X_i}{Y_i}\right|\times100\% \quad (14)$$

where N is the total number of statistical experimental data; X_i and Y_i are the stresses predicted by the equation and the corrected one obtained from the experiment, respectively. The correlation between the experimental and the predictive values is shown in Fig. 9. AARE and R_1

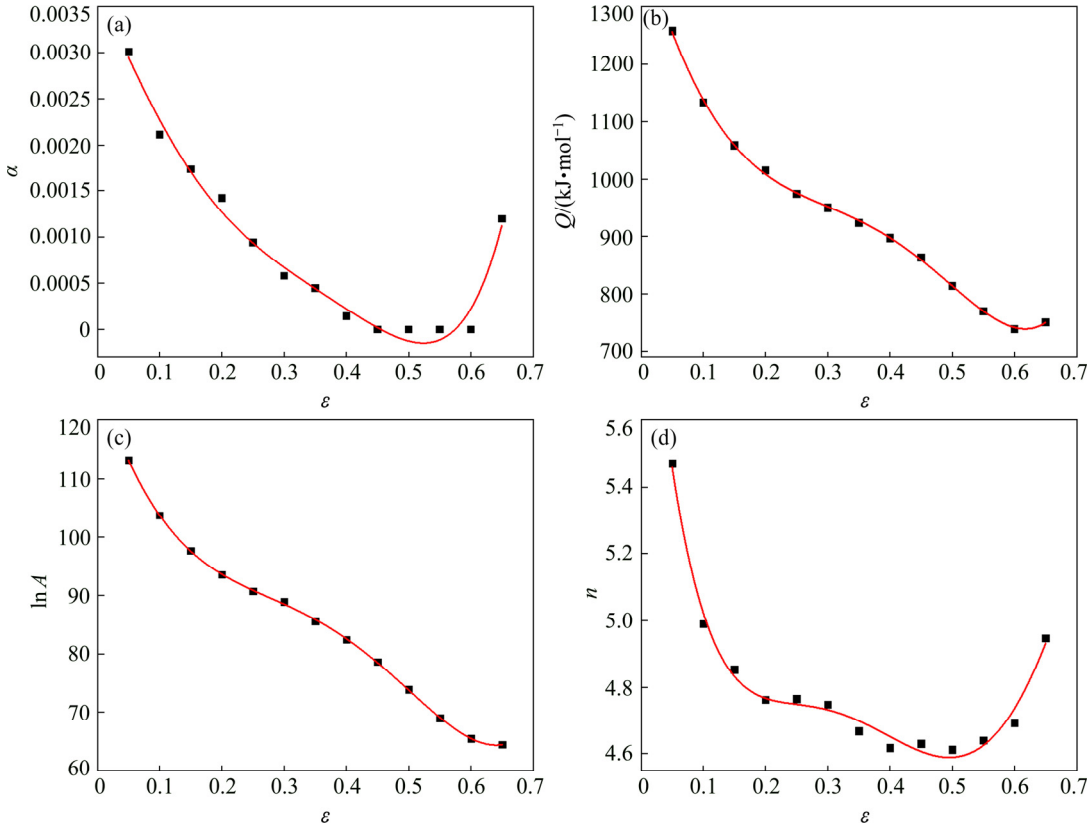

Fig. 7 Dependence of material parameters in constitutive equation of experimental superalloy on true strain: (a) α; (b) Q; (c) ln A; (d) n

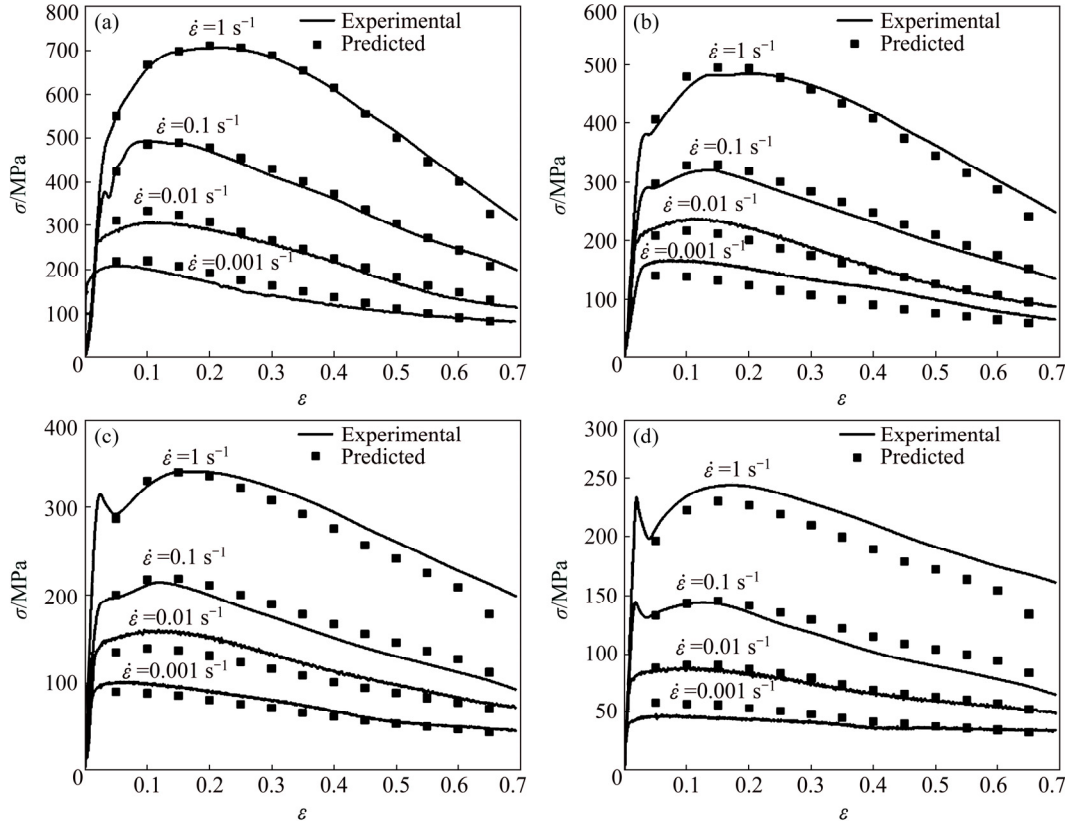

Fig. 8 Corrected flow stress curves by experiments and predictive stresses of experimental superalloy compressed at different temperatures: (a) 1020 °C; (b) 1050 °C; (c) 1080 °C; (d) 1110 °C

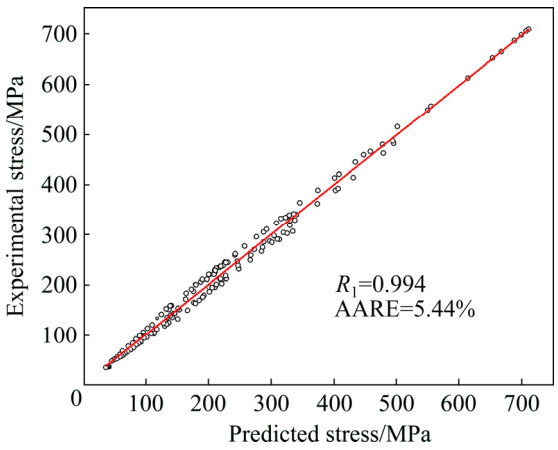

Fig. 9 Correlation between experimental and predicted flow stress for superalloy

are determined to be 5.44% and 0.994, respectively, which indicate that the flow stress of the superalloy during hot deformation can be effectively predicted by the constitutive equation established in this work.

3.4 Hot processing map

Hot processing map established on the basis of the dynamic materials model (DMM) has been used for the optimization of processing parameters and prediction of unstable regions during hot working of PM superalloys [3,8−10]. In accordance with the theory of DMM, the deformed material is regarded as a nonlinear power dissipator. The dissipative energy P consists of two parts: the dissipative power during plastic work (G content) and the dissipative power during microstructural evolution (J co-content). Thus, P can be expressed as [32]

$$P=\sigma\dot{\varepsilon}=G+J=\int_0^{\dot{\varepsilon}}\sigma \mathrm{d}\dot{\varepsilon}+\int_0^{\sigma}\dot{\varepsilon}\mathrm{d}\sigma \tag{15}$$

The stress of materials is rate sensitive, which can be represented as

$$\sigma=k\dot{\varepsilon}^{m} \tag{16}$$

where k is a constant; m denotes the strain rate sensitivity.

In order to characterize the dissipative power through the microstructural evolution of materials during hot deformation, the efficiency of power dissipation η, which is a dimensionless parameter, is defined and derived as a function of strain rate sensitivity (m):

$$\eta=\frac{J}{J_{\max}}=\frac{2m}{2m+1} \tag{17}$$

The power dissipation map which is presented in the form of an equivalent 2D map can be obtained by plotting the contours of η under various deformation conditions. Since instability phenomena, such as adiabatic, flow localization, intergranular and wedge cracks [33,34], may also occur during hot working of materials, an instability criterion was proposed by PRASAD and SESHA-CHARYULU [35] according to the extremum principles of irreversible thermodynamics. An instability parameter $\xi(\dot{\varepsilon})$, which is related to $\dot{\varepsilon}$ and T, is defined to identify the regime of flow instability:

$$\xi(\dot{\varepsilon})=\frac{\partial \ln[m/(m+1)]}{\partial \ln \dot{\varepsilon}}+m<0 \tag{18}$$

The instability map that shows the regions where $\xi(\dot{\varepsilon})$ is negative can be constituted according to Eq. (18). Thus, by overlapping the instability map on the power dissipation map, the hot processing maps can be constructed.

3.4.1 Stability and instability domains

For the experimental superalloys deformed at strains of 0.2, 0.4, 0.6 and 0.7 within the temperatures from 1020 to 1110 °C under the strain rates from 0.001 to 1 s^{-1}, the hot processing maps are established, as seen from Fig. 10. In general, the η value reflects the microstructural mechanism of the deformed materials in the domain corresponding to particular deformation conditions. According to Fig. 10, the η value of the alloy varies with the true strain in the domain with the same strain rate and temperature, which indicates that different mechanisms of microstructural evolution occurred with the deformation proceeding. Since the strain of 0.7 is closest to the actual forging condition, the map corresponding to the strain of 0.7 was further analyzed. It is found from Fig. 10(d) that there exist three different domains with peak efficiencies. The first domain is within the temperatures of 1020−1030 °C and strain rates of $10^{-2.5}$−$10^{-1.5}$ s^{-1}, with a maximum η of about 42% occurring at about 1020 °C and 10^{-2} s^{-1}. The second domain is within the temperatures of 1075−1110 °C and strain rates of $10^{-0.4}$−1 s^{-1}, with a maximum η of ~47% occurring at about 1110 °C and 10^{-3} s^{-1}. The third domain is within the temperatures of 1075−1105 °C and strain rates of 10^{-3}−$10^{-2.8}$ s^{-1}, with a maximum η of about 61% occurring at about 1095 °C and 10^{-3} s^{-1}. High η domains usually imply

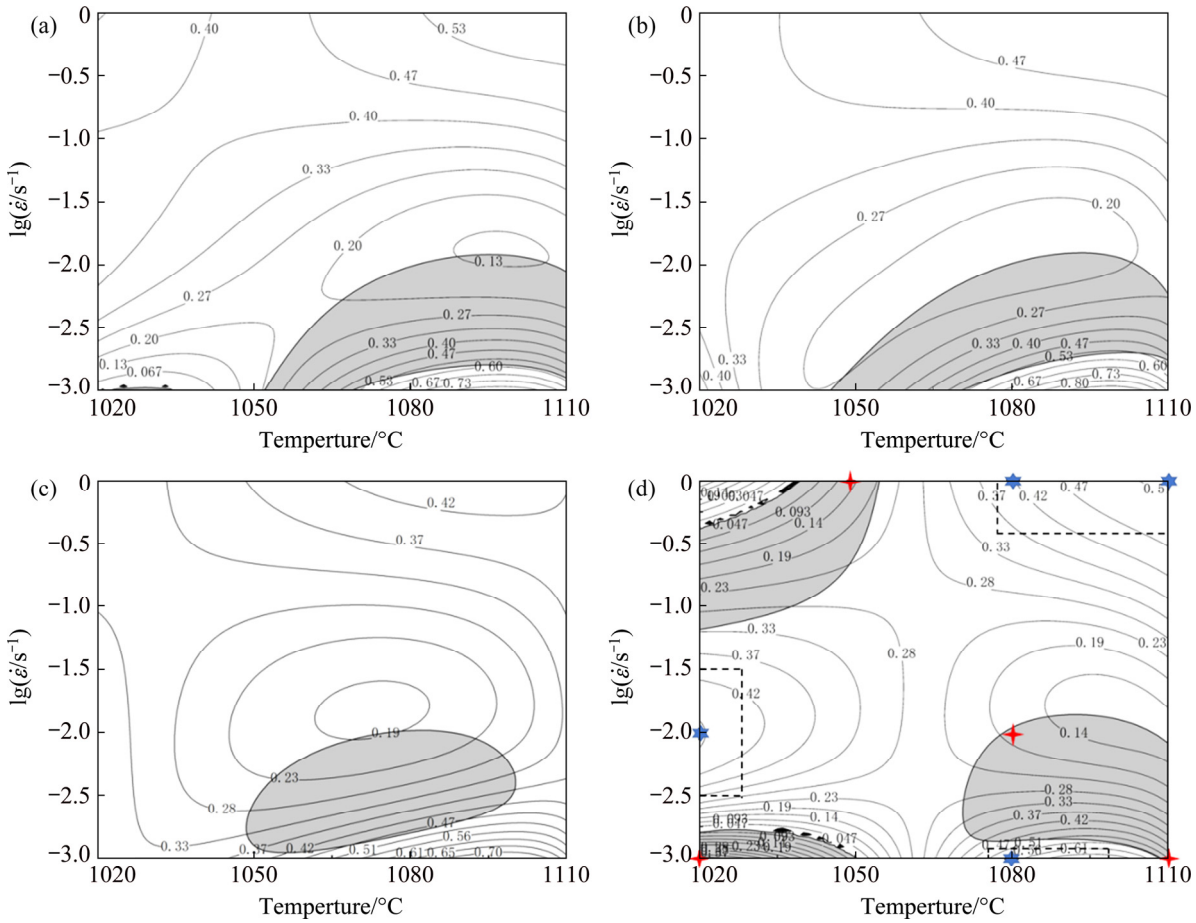

Fig. 10 Hot processing maps of experimental superalloy compressed at different true strains: (a) ε=0.2; (b) ε=0.4; (c) ε=0.6; (d) ε=0.7

that the most efficiently microstructural evolution happens in the materials during hot working. Thus, the three domains with peak efficiencies obtained above are considered as the candidate domains for hot working.

It may be noted from Fig. 10 that in the hot processing maps, the instability domains expand as the true strain increases (see grey regions in the maps). For the map corresponding to a true strain of 0.7 (Fig. 10(d)), three instability domains are exhibited. The first one locates within the temperatures of 1020−1055 °C and the strain rates of $10^{-1.2}$−1 s^{-1}. The second one mainly occurs at the temperatures below 1050 °C and the strain rates less than $10^{-2.75}$ s^{-1}. The third one is mainly situated within the temperatures of 1070−1110 °C and the strain rates of $10^{-2.7}$−$10^{-1.8}$ s^{-1}. During hot working of the superalloy, the three instability domains should be avoided.

3.4.2 Microstructure mechanism

Figure 11 shows the optical micrographs of specimens deformed under different conditions corresponding to the marks in Fig. 10(d). DRX has already occurred at the strain rate of 1 s^{-1}, and “necklace” type microstructure is exhibited with the elongated grains surrounded by fine equiaxed grains, especially at low temperatures (Figs. 11(a−c)). The amount of DRX grains increases with elevating temperature. However, since insufficient deformation time may restrain the DRX process at high strain rate, the DRX fraction at different temperatures remains at a low level. The “necklace” type microstructures are still apparent at the strain rate of 0.01 s^{-1} (Figs. 11(d) and (e)), and the fraction of DRX increases to various degrees under different temperatures. With the strain rate decreasing to 0.001 s^{-1} (see Figs. 11(f−h)), fully recrystallized microstructure is revealed at the temperature of 1080 °C (Fig. 11(g)). When the temperature rises to 1110 °C, coarse recrystallized grain is detected (Fig. 11(h)), because more time can be provided for DRX at lower strain rate, causing the growth of recrystallized grains [14].

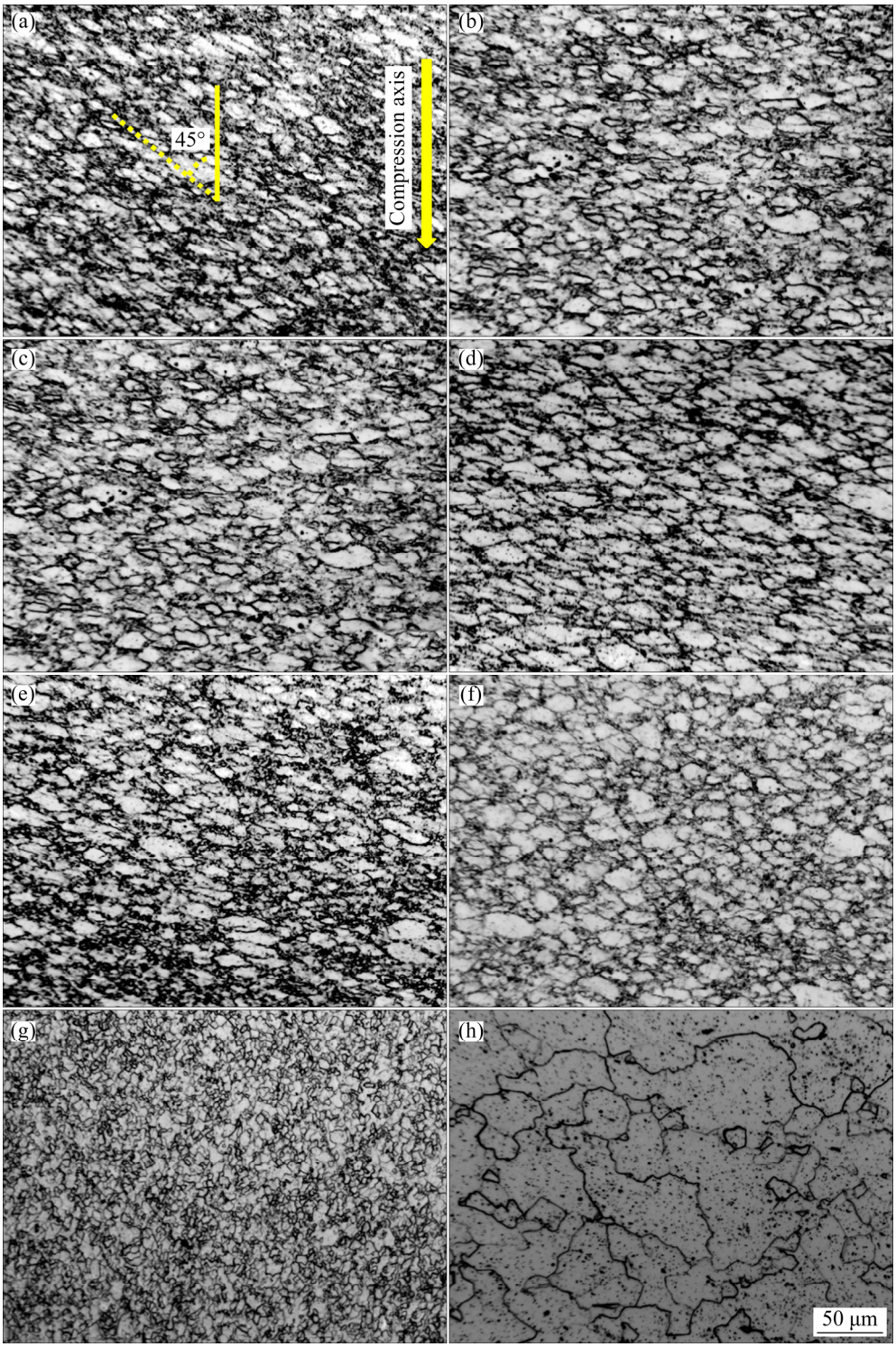

Fig. 11 Microstructures of experimental superalloys compressed under different conditions: (a) 1050 °C, 1 s^{-1}; (b) 1080 °C, 1 s^{-1}; (c) 1110 °C, 1 s^{-1}; (d) 1020 °C, 0.01 s^{-1}; (e) 1080 °C, 0.01 s^{-1}; (f) 1020 °C, 0.001 s^{-1}; (g) 1080 °C, 0.001 s^{-1}; (h) 1110 °C, 0.001 s^{-1}

In order to analyze the reasons for the instability of the experimental alloy, the microstructures of the representative specimens with deformation conditions corresponding to the instability domains were further examined. In the first instability domain (t=1020−1055 °C, $\dot{\varepsilon}=10^{-1.2}$−1 s^{-1}), some typical failure features of the nickel-based superalloys compressed at high strain rates are exhibited, which are characterized by the formation of adiabatic shear bands at an angle

of approximate 45° from the compression axis (Fig. 11(a)). At higher strain rates ($\dot{\varepsilon} \geq 0.1$ s^{-1}), the deformation heat generated by the core of the sample during hot compression cannot be released in a timely manner because of the low thermal conductivity of superalloys, resulting in the localized temperature rises [36]. The bands of flow localization are thus formed, leading to the occurrence of flow instability. Microstructural observation in the second instability domain (t=1020−1050 °C, $\dot{\varepsilon}$ =10^{-3}−$10^{-2.75}$ s^{-1}) indicates that the intergranular cracks occur along the grain boundaries (Fig. 12(a)). The large resistance to deformation at low temperatures makes the dislocations easily entangled at the grain boundaries and PPB or other defects, causing the rise in local stress so as to promote the formation of intergranular cracking [37]. In the third instability domain (t=1070−1110 °C, $\dot{\varepsilon}$ =$10^{-2.7}$−$10^{-1.8}$ s^{-1}), intergranular cracking and wedge cracking are demonstrated to be dominant, which are presented in Figs. 12(b) and (c), respectively. Wedge cracking appears primarily at triple junctions and propagates along grain boundaries. Under high temperature conditions, the coarsened grains lead to poor coordination between grains, which would hinder the grain boundary slip. The stress concentration and wedge cracks at the trigeminal boundary are more likely to emerge [38]. The microstructural characteristics above should be avoided in hot processing, since they are undesirable in achieving uniform mechanical properties.

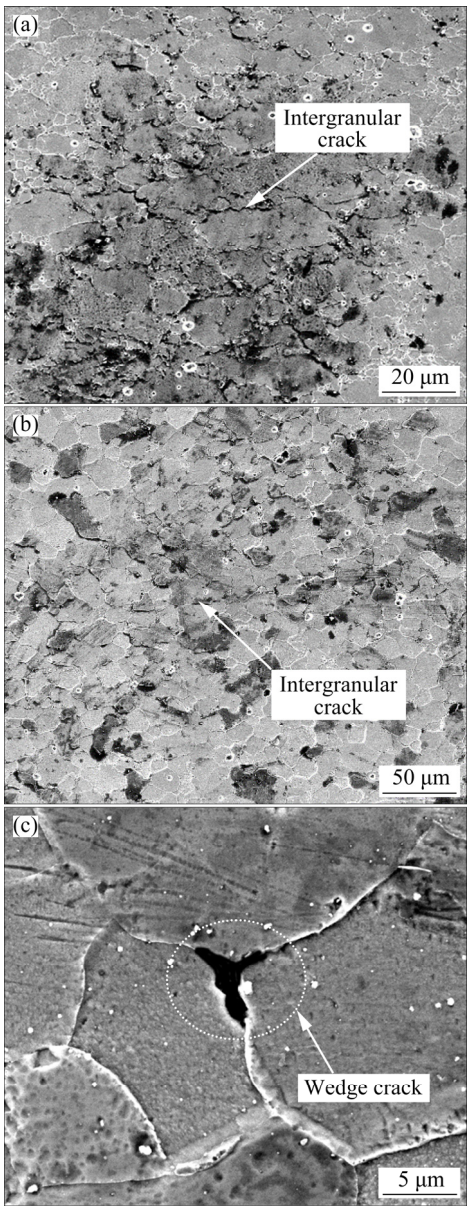

Fig. 12 Microstructures of experimental superalloys compressed in instability domains corresponding to different conditions: (a) 1020 °C, 0.001 s^{-1}; (b) 1080 °C, 0.01 s^{-1}; (c) 1110 °C, 0.001 s^{-1}

According to the interpretations above, Fig. 13 shows the constituent features in various domains. Based on the dissipation efficiency η and microstructural analyses, the optimal processing parameters for the experimental superalloy under the strain of 0.7 are suggested to be under the conditions within the temperatures of 1075−1105 °C and the strain rate of 10^{-3}−$10^{-2.8}$ s^{-1}. A peak efficiency of about 61% is exhibited, and favorable DRX microstructure and excellent workability are expected in the domains.

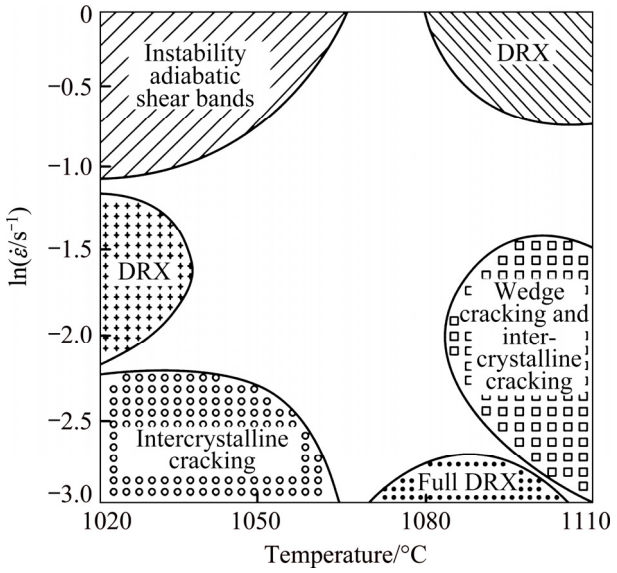

Fig. 13 Various domains corresponding to microstructural mechanisms of experimental superalloy during hot working as predicted by hot processing map

4 Conclusions

(1) Classic characteristics of DRX are exhibited in the flow curves of the superalloy. The flow stress presents a decreasing trend as the temperature increases and the strain rate decreases.

(2) For hot compression of the superalloy, the activation energy is determined to be 1111.3 kJ/mol. Based on the peak stress corrected by friction and temperature rise, the constitutive equation has been developed.

(3) Three instability domains are depicted in the processing map of the superalloy under the strain of 0.7. The adiabatic shear band, intergranular crack and a combination of intergranular crack and wedge crack are demonstrated to be responsible for the instabilities corresponding to three domains of t=1020−1055 °C and $\dot{\varepsilon}=10^{-1.2}$−1 s^{-1}, t=1020−1050 °C and $\dot{\varepsilon}=10^{-3}$−$10^{-2.75}$ s^{-1}, t=1070−1110 °C and $\dot{\varepsilon}=10^{-2.7}$−$10^{-1.8}$ s^{-1}, respectively.

(4) The optimal isothermal forging conditions for the superalloy is determined to be t=1075−1105 °C and $\dot{\varepsilon}=10^{-3}$−$10^{-2.8}$ s^{-1}.

References

[1] VISWANATHAN G B, SAROSI P M, HENRY M F, WHITIS D D, MILLIGAN W W, MILLS M J. Investigation of creep deformation mechanisms at intermediate temperatures in René 88 DT [J]. Acta Materialia, 2005, 53: 3041−3057.

[2] WANG Yan, SHAO Wen-zhou, ZHEN Liang, ZHANG Bao-you. Hot deformation behavior of delta-processed superalloy 718 [J]. Materials Science and Engineering A, 2011, 528: 3218−3227.

[3] XU Wei, ZHANG Li-wen, GU Sen-dong, ZHANG Jian-lin. Hot compressive deformation behavior and microstructure evolution of HIPed FGH96 superalloy [J]. Transactions of Nonferrous Metals Society of China, 2012, 22: 66−71.

[4] ALNIAK M O, BEDIR F. Modelling of deformation and microstructural changes in P/M Rene 95 under isothermal forging conditions [J]. Materials Science and Engineering A, 2006, 429: 295−303.

[5] CHEN Xiao-min, LIN Y C, WEN Dong-xu, ZHANG Jin-long, HE Min. Dynamic recrystallization behavior of a typical nickel-based superalloy during hot deformation [J]. Materials and Design, 2014, 57: 568−577.

[6] KANG Fu-wei, ZHANG Guo-qing, LI Zhou, SUN Jian-fei. Hot deformation of spray formed nickel-base superalloy using processing maps [J]. Transactions of Nonferrous Metals Society of China, 2008, 18: 531−535.

[7] WANG Yan, SHAO Wen-zhou, ZHEN Liang, YANG Li, ZHANG Xin-mei. Flow behavior and microstructures of superalloy 718 during high temperature deformation[J]. Materials Science and Engineering A, 2008, 497: 479−486.

[8] NING Y Q, YAO Z K, YANG Z, GUO H Z, FU M W. Flow behavior and hot workability of FGH4096 superalloys with different initial microstructures by using advanced processing maps [J]. Materials Science and Engineering A, 2012, 531: 91−97.

[9] SUI Feng-li, XU Li-xia, CHEN Li-qing, LIU Xiang-hua. Processing map for hot working of Inconel 718 alloy [J]. Journal of Materials Processing Technology, 2011, 211: 430−440.

[10] HE Guo-ai, LIU Feng, SI Jia-yong, YANG Chuang, JIANG Liang. Characterization of hot compression behavior of a new HIPed nickel-based P/M superalloy using processing maps [J]. Materials and Design, 2015, 87: 256−265.

[11] PAN Q L, LI B, WANG Y, ZHANG Y W, YIN Z M. Characterization of hot deformation behavior of Ni-base superalloy Rene'41 using processing map [J]. Materials Science and Engineering A, 2013, 585: 371−378.

[12] LI Hui-zhong, YANG Lei, WANG Yan, TAN Gang, QIAO Shi-chang, HUANG Zheng-qin, LIU Min-xue. Thermal deformation and dynamic recrystallization of a novel HEXed P/M nickel-based superalloy [J]. Materials Characterization, 2020, 163: 110285.

[13] WANG Yan, ZHEN Liang, SHAO Wen-zhou, YANG Li, ZHANG Xin-mei. Hot working characteristics and dynamic recrystallization of delta-processed superalloy 718 [J]. Journal of Alloys and Compounds, 2009, 474: 341−346.

[14] LIU Yan-hui, NING Yong-quan, YAO Ze-kun, GUO Hong-zhen, NAN Yang. Effect of true strains on processing map for isothermal compression of Ni−20.0Cr−2.5Ti−1.5Nb−1.0Al Ni-base superalloy [J]. Journal of Alloys and Compounds, 2014, 612: 56−63.

[15] JARRETT R N, TIEN J K. Effects of cobalt on structure, microchemistry and properties of a wrought nickel-base superalloy [J]. Metallurgical Transactions A, 1982, 13: 1021−1032.

[16] NING Y Q, YAO Z K, FU M W, GUO H Z. Recrystallization of the hot isostatic pressed nickel-base superalloy FGH4096: I. Microstructure and mechanism [J]. Materials Science and Engineering A, 2011, 528: 8065−8070.

[17] LI De-fu, GUO Qing-miao, GUO Sheng-li, PENG Hai-jian, WU Zhi-guang. The microstructure evolution and nucleation mechanisms of dynamic recrystallization in hot-deformed Inconel 625 superalloy [J]. Materials and Design, 2011, 32: 696−705.

[18] LIANG Xiao-peng, LIU Yang, LI Hui-zhong, ZHOU Can-xu, XU Guo-fu. Constitutive relationship for high temperature deformation of powder metallurgy Ti−47Al−2Cr−2Nb−0.2W alloy [J]. Materials and Design, 2012, 37: 40−47.

[19] EBRAHIMI R, NAJAFIZADEH A. A new method for evaluation of friction in bulk metal forming [J]. Journal of Materials Processing Technology, 2004, 152: 136−143.

[20] ZHANG Jian-sheng, XIA Yu-feng, QUAN Guo-zheng, WANG Xuan, ZHOU Jie. Thermal and microstructural softening behaviors during dynamic recrystallization in 3Cr20Ni10W2 alloy [J]. Journal of Alloys and Compounds, 2018, 743: 464−478.

[21] GOETZ R L, SEMIATIN S L. The adiabatic correction factor for deformation heating during the uniaxial compression test [J]. Journal of Materials Engineering and Performance, 2001, 10: 710−717.
[22] LI L X, ZHOU J, DUSZCZYK J. Determination of a constitutive relationship for AZ31B magnesium alloy and validation through comparison between simulated and real extrusion [J]. Journal of Materials Processing Technology, 2006, 172: 372−380.
[23] SELLARS C M, MCTEGART W J. On the mechanism of hot deformation [J]. Acta Metallurgica, 1966, 14: 1136−1138.
[24] ZENER C, HOLLOMON J H. Effect of strain rate upon plastic flow of steel [J]. Journal of Applied Physics, 1944, 15: 22−32.
[25] ZHANG Ming-jie, LI Fu-guo, WANG Shu-yun, LIU Chen-yi. Effect of powder preparation technology on the hot deformation behavior of HIPed P/M nickel-base superalloy FGH96 [J]. Materials Science and Engineering A, 2011, 528: 4030−4039.
[26] GU Y, HARADA H, CUI C, PING D, SATO A, FUJIOKA J. New Ni−Co-base disk superalloys with higher strength and creep resistance [J]. Scripta Materialia, 2006, 55: 815−818.
[27] GAZDA A, ROTHOVA V, CERMAK J. Interdiffusion in pseudobinary sections of Ni3Al−Co ternary system [J]. Intermetallics, 2002, 10: 859−864.
[28] LEVERANT G R, KEAR B H. The mechanism of creep in gamma prime precipitation-hardened nickel-base alloys at intermediate temperatures [J]. Metallurgical and Materials Transactions B, 1970, 1: 491−498.
[29] NA Y S, YEOM J T, PARK N K, LEE J Y. Simulation of microstructures for alloy 718 blade forging using 3D FEM simulator [J]. Journal of Materials Processing Technology, 2003, 141: 337−342.
[30] LI Fu-lin, FU Rui, YIN Fa-jie, FENG Di, WANG Hai-zhou, DU Gang, FENG Yong. Impact of $\gamma'(Ni_3(Al,Ti))$ phase on dynamic recrystallization of a Ni-based disk superalloy during isothermal compression [J]. Journal of Alloys and Compounds, 2017, 693: 1076−1082.
[31] ZHANG Peng, HU Chao, ZHU Qiang, DING Chao-gang, QIN He-yong. Hot compression deformation and constitutive modeling of GH4698 alloy [J]. Materials and Design, 2015, 65: 1153−1160.
[32] PRASAD Y V R K, GEGEL H L, DORAIVELU S M, MALAS J C, MORGAN J T, LARK K A, BARKER D R. Modeling of dynamic material behavior in hot deformation: Forging of Ti-6242 [J]. Metallurgical Transactions A, 1984, 15: 1883−1892.
[33] MURTY S V S N, RAO B N. On the development of instability criteria during hot working with reference to IN718 [J]. Materials Science and Engineering A, 1998, 254: 76−82.
[34] NARAYANA S V S M, NAGESWARA B R, KASHYAP B P. Instability criteria for hot deformation of materials [J]. International Materials Reviews, 2000, 45: 15−26.
[35] PRASAD Y V R K, SESHACHARYULU T. Modelling of hot deformation for microstructural control [J]. International Materials Reviews, 1998, 43: 243−258.
[36] PENG Wen-wen, ZENG Wei-dong, WANG Qing-jiang, YU Han-qing. Characterization of high-temperature deformation behavior of as-cast Ti60 titanium alloy using processing map [J]. Materials Science and Engineering A, 2013, 571: 116−122.
[37] BROOKS J W. Forging of superalloys [J]. Materials and Design, 2000, 21: 297−303.
[38] EDINGTON J W, MELTON K N, CUTLER C P. Superplasticity [J]. Progress in Materials Science, 1976, 21: 61−170.

一种热挤压态粉末镍基高温合金在热压缩过程中的热加工特性

谭 钢[1]，李慧中[1]，王 岩[2,3]，杨 雷[1]，乔世昌[3]，黄钰钦[3]，刘敏学[4]

1. 中南大学 材料科学与工程学院，长沙 410083；2. 哈尔滨工业大学 金属精密加工国家重点实验室，哈尔滨 150001；
3. 中南大学 航空航天学院，长沙 410083；4. 中南大学 粉末冶金国家重点实验室，长沙 410083

摘 要：为了研究新型粉末冶金镍基高温合金的热变形行为，在变形温度为 1020~1110 °C、应变速率为 0.001~1 s^{-1} 条件下进行热压缩试验。结果表明，高温合金的流动应力随着变形温度的升高和应变速率的降低而减小。通过双曲正弦型函数表达式建立精准的本构方程。此外，构造合金的热加工图以优化其热锻参数。在应变量为 0.7 的热加工图中分别确定动态再结晶稳定和失稳的 3 个区域。绝热剪切带、晶间裂纹以及晶间裂纹和楔形裂纹的结合被证明是造成失稳的原因。综合分析热加工图和显微组织，确定高温合金的最佳等温锻造条件为 t=1075~1105 °C 和 $\dot{\varepsilon}=10^{-3}$~$10^{-2.8}$ s^{-1}。

关键词：粉末冶金；镍基高温合金；热变形行为；本构方程；热加工图；动态再结晶

(Edited by Wei-ping CHEN)